CrossMark

JFM RAPIDS
journals.cambridge.org/rapids

Bending oscillations of a cylinder freely falling in still fluid

Patricia Ern[1],†, Jérôme Mougel[1], Sébastien Cazin[1], Manuel Lorite-Díez[1]
and Rémi Bourguet[1]

[1]Institut de Mécanique des Fluides de Toulouse (IMFT), CNRS, Université de Toulouse, France

We investigate experimentally the behaviour of an elongated flexible cylinder settling at moderate Reynolds number under the effect of buoyancy in a fluid otherwise at rest. The experiments uncover the development of large-amplitude periodic deformations of the cylinder (of the order of its diameter) in specific parameter ranges. Bending oscillations are observed to occur for two base flow situations, involving either a steady or an unsteady wake. In both cases, the sequence of oscillatory deformations emerging when the cylinder length is increased involves the bending modes of an unsupported cylinder with free ends. Comparison of the deformation frequency measured for the falling cylinder with the vortex shedding frequency expected for a non-deformable cylinder at the same Reynolds number indicates that the deformation is coupled to the wake unsteadiness. It also suggests that the cylinder degrees of freedom in deformability allow wake instability to be triggered at Reynolds numbers that would be subcritical for fixed rigid cylinders.

Key words: flow–structure interactions, wakes

1. Introduction

The behaviour of single bodies freely rising or falling under the effect of buoyancy in a fluid at rest has attracted growing interest in the last 20 years, leading to a better understanding of the roles of wake instability and of body anisotropy on the occurrence of non-rectilinear paths (see e.g. Ern *et al.* 2012). However, for a deformable body, the coupling of its deformation with both its path and its wake remains widely unexplored, with a few rare exceptions. Among these, the freely rising bubble appears as a paradigmatic case, as it provides a series of advances concerning the impact of mean and oscillatory shape deformations on the onset of path instability (Mougin & Magnaudet 2002; Cano-Lozano *et al.* 2016; Bonnefis 2019), on path characteristics (Filella, Ern &

† Email address for correspondence: ern@imft.fr

905 R5-1

Roig 2015) and on wake structure (Veldhuis, Biesheuvel & van Wijngaarden 2008), to cite just a few results and references.

In the case of solid flexible bodies freely moving in a low-viscosity fluid, only a few studies have dealt with the coupling between path and deformation of the body. Tam *et al.* (2010) investigated the mean reconfiguration to an arched shape of a tumbling rectangular flexible paper strip freely falling in air and the resulting increase in descent rate. They showed that the transition from straight to bent configuration occurs when the destabilizing inertial force induced by the angular velocity of the tumbling strip overbalances the bending resistance of the body. The influence of flexibility on the fluttering motion of a falling strip was investigated by Tam (2015). They observed localized upward bending deformations, generally not exceeding 5 % of the chord length, during short time intervals close to the turning points of the path, the strip remaining flat during intermediate gliding periods. He showed, in turn, that the observed deformation resulted in increased lift, and therefore in a lower descent rate, and induced shedding of stronger vortices than in the case of stiff plates. At variance with the case of the bubble, the literature on freely falling flexible bodies is thus far limited to situations bringing to light flow-induced reconfigurations, in the form of either a steady or a transitory deformation.

Such behaviours for freely moving objects are the counterpart of the deformation response observed for partially fixed or locally restrained bodies immersed in a flow. For instance, shape adaptation can be traced in the leaning of an elongated flexible cylinder held at one end under the effect of a steady current (Leclercq & de Langre 2018), or in the stationary draping featuring multiple lobes observed for a soft disc held in its centre in an incoming flow, for both steady and unsteady wakes (Schouveiler & Eloy 2013; Hua, Zhu & Lu 2014). However, studies also revealed the occurrence of time-periodic deformations of the body associated with vortex shedding, for instance in the case of a flexible plate clutched at its centre (Pfister, Marquet & Carini 2019). Also, a flexible cylinder held from its ends and placed in flowing fluid exhibits vibrations that are driven by the synchronization between body deformation and flow unsteadiness (Chaplin *et al.* 2005; Bourguet, Karniadakis & Triantafyllou 2011; Gedikli, Chelidze & Dahl 2018; Seyed-Aghazadeh, Edraki & Modarres-Sadeghi 2019). These vibrations, often referred to as vortex-induced vibrations, may involve several structural modes, sometimes simultaneously (Bourguet, Karniadakis & Triantafyllou 2013). Their amplitudes are typically of the order of one body diameter in the cross-flow direction and one or more orders of magnitude lower in the streamwise direction.

Oscillatory deformations may therefore be expected to develop in the case of a freely falling body, as happens for bubbles or restrained bodies. Following this view, we focused our attention on a flexible cylinder settling under the influence of gravity in still fluid, and investigated experimentally the influence of flexibility on its freely falling motion over a range of elongation ratios. The present paper brings to light the onset of oscillatory deformations for two distinct flow situations, both corresponding to rigid-body motions of an undeformed cylinder falling with its axis perpendicular to gravity. In the first one, periodic deformations set in for a cylinder in rectilinear fall with a steady wake. In the second one, they arise for a flexible cylinder undergoing an azimuthal oscillatory motion coupled with an unsteady wake.

2. Experimental approach

We consider a circular cylinder of diameter d, length L, density $\rho_c \simeq 1160$ kg m^{-3} and Young modulus $E \simeq 1$ MPa falling through quiescent water (density $\rho_f \simeq 1000$ kg m^{-3},

kinematic viscosity $\nu \simeq 10^{-6}$ m s^{-2}) under the influence of gravitational acceleration g. The problem is governed by four dimensionless parameters, including the solid-to-fluid density ratio $m^* = \rho_c/\rho_f$ and the elongation ratio of the cylinder L/d. We next introduce the gravitational velocity $V_g = \sqrt{(m^* - 1)gd}$, which was shown by Toupoint, Ern & Roig (2019) to be the relevant velocity scale for the buoyancy-driven fall of cylinders in a comparable range of control parameters. Comparing this free-fall velocity with the velocity V_c associated with the bending modes of a finite-length cylinder (with a potential added-mass coefficient of 1) provides the dimensionless parameter called 'velocity ratio' U^* accounting for the body deformability, such that

$$U^* = \frac{V_g}{V_c} \quad \text{with} \quad V_c = f_0 L \quad \text{and} \quad f_0 = \frac{d}{L^2}\sqrt{\frac{E}{\rho_c + \rho_f}}. \qquad (2.1a,b)$$

Last, we introduce the Archimedes number Ar balancing buoyancy and viscosity effects, $Ar = V_g d/\nu$. Note that, once the mean fall velocity U of the cylinder is determined from experiments, the Reynolds number $Re = Ud/\nu$ can be defined, for comparison with the case of fixed bodies embedded in an incoming flow.

The procedure followed is to start the series of experiments with a long cylinder (typically $L \simeq 120$ mm for a cylinder with $d = 1$ mm) and to gradually decrease its length by steps of 5 mm. This results in a joint variation of L/d and U^*, while m^* and Ar are kept constant. We operated two methods of release of the flexible cylinders, in order to investigate the impact of initial conditions on the cylinder behaviour and to test the robustness of the phenomenon uncovered. Both methods used immersed bodies to avoid the presence of bubbles on the body surface. The first one consisted in releasing the cylinder hold straight from both ends. The second one intended to ensure no tension of the cylinder at release, and consisted in delicately pushing with a thin long-enough plate the body lying straight on a diving-board. Both methods provided the same observations, indicating that the origin of the oscillatory deformations is not related to prestressing. In both configurations, we could not avoid a slight initial inclination of the body at release. Inclination angles relative to horizontal are in all cases less than $7°$, and in most cases less than $4°$. The resulting lateral drift of the body (less than 7 % of the mean vertical velocity) decreased with the progressive slipping towards horizontality of the body due to the added-mass torque (see, for instance, Ern *et al.* (2012), for a discussion on the role of this torque). Regardless of the release conditions, we observed that the deformations are robust with respect to the presence of a weak drift, as phase locking between the oscillations of the two ends of the cylinder was preserved despite path asymmetry. The inclination angle may, however, affect the amplitude of oscillation and the drag coefficient, as will be discussed later.

Recordings of the falling cylinders were performed by shadowgraphy with two synchronized scientific complementary metal-oxide-semiconductor (sCMOS) cameras, 2560×2160 pixels (px), at a frequency of 50 Hz and placed in front of two 20 cm $\times$ 20 cm backlight flat panels producing directional illumination. A sketch of the experimental configuration is provided in figure 1. One camera imaged a field of view of 122 mm $\times$ 103 mm in a vertical plane (which limits the length of the cylinders), and the second camera imaged a region of 167 mm $\times$ 141 mm in a horizontal plane thanks to a mirror inclined at $45°$.

For elongated bodies such as those considered here, important distortion effects on the body shape arise with perspective vision, as the body is unavoidably inclined in an angular field of view and off-centre relative to the line of sight of the camera. To disentangle
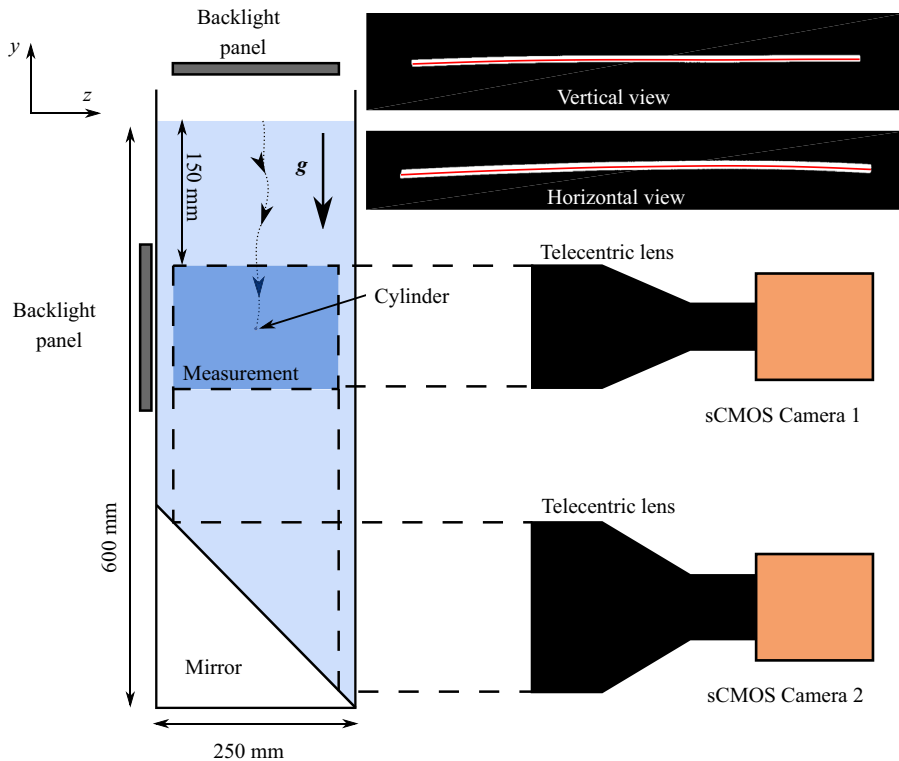
FIGURE 1. Sketch of the experimental set-up, showing the positions of the cameras, the measurement volume in the square-section water tank, along with a qualitative picture of the falling cylinder. Cropped binarized images from both cameras obtained by image processing are also displayed, and show the centreline of the cylinder contour (red line).

the contributions to the cylinder behaviour of the different degrees of freedom is then an awkward procedure, even for rigid bodies, which is often resolved by capturing and reprojecting two generatrices of the cylinder (Toupoint *et al.* 2019). In the case of a deforming body, this routine can no longer be employed straightforwardly.

To solve the problem, we used telecentric lenses, which combine several advantages: magnification and spatial resolution (typically, 15.3 px mm^{-1} for the horizontal plane and 21 px mm^{-1} for the vertical one) are invariant along the depth of field (telecentricity depth), parallax is avoided, and distortion is lower than with standard lenses. Calibration is carried out by recording a fixed object of known dimensions at different locations in the cubic measurement volume, confirming the constant magnification in the field of view (variations below 0.1 px). The analysis of body displacements and deformations in time in the vertical and horizontal planes is performed by image processing, in particular to track the mean centreline of the cylinder (figure 1).

3. General observations and results

We first consider the case of a cylinder falling with a mean vertical velocity corresponding to $Re \simeq 42$ ($d = 1$ mm). For sufficiently short cylinders, no deformation is visible. The cylinder maintains a straight conformation, falling with its axis perpendicular
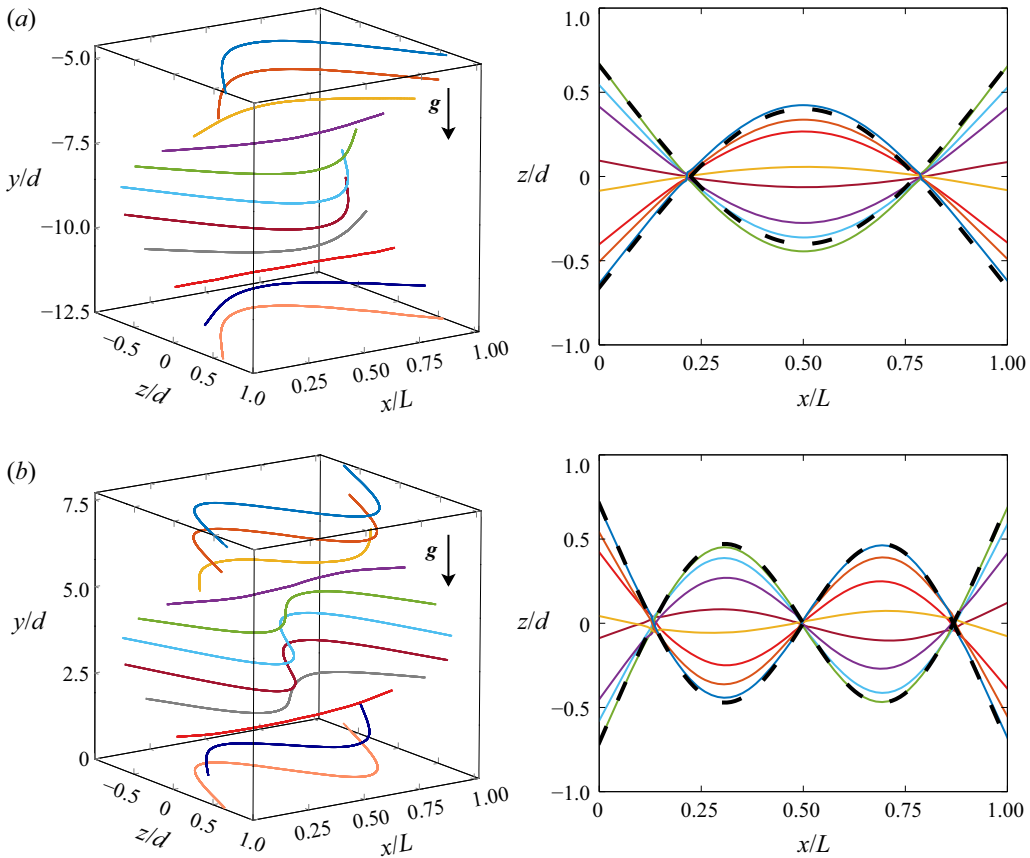
FIGURE 2. Illustrations of the bending oscillatory deformations of a cylinder (with $d = 1$ mm): (a) M_1 ($L/d = 70$) and (b) M_2 ($L/d = 110$). The left panels show three-dimensional views, with y standing for the vertical coordinate. The right panels show the deformation in the horizontal (x, z) plane, with x describing the undeformed cylinder axis and z the transverse direction. The dashed black lines outline the envelope given by (3.1) with an amplitude adjusted to that of the cylinder ends in the experiments.

to gravity like a rigid cylinder. For $L/d \simeq 57$, the path of the cylinder can be considered as rectilinear, since only very weak non-reproducible irregular horizontal displacements are recorded (less than 3 % of d), as is commonly the case in experiments with freely moving objects (see discussions in Ern *et al.* (2012) and Toupoint *et al.* (2019)).

However, as the elongation ratio of the cylinder increases, a sequence of periodic deformations emerges. For L/d larger than approximately 60, a time-periodic deformation of the cylinder sets in. It is composed of one crest and two nodes, as illustrated in figure 2(a). It will be termed M_1 in reference to the corresponding bending mode of a beam. As L/d is further increased, the amplitude of deformation grows, reaches a maximum for $L/d \simeq 70$ (value at the cylinder ends of approximately $0.66d$ and span-averaged value of $0.3d$), and decreases beyond. Oscillatory deformation M_1 is observed until $L/d \simeq 95$, featuring a displacement amplitude at the cylinder ends of $0.22d$ and a span-averaged value of $0.15d$. For $L/d \simeq 98$, the cylinder switches to M_2 (in reference to mode 2), characterized by two crests and three nodes, as illustrated in figure 2(b). The amplitude at the cylinder ends is then $0.37d$ (span-averaged
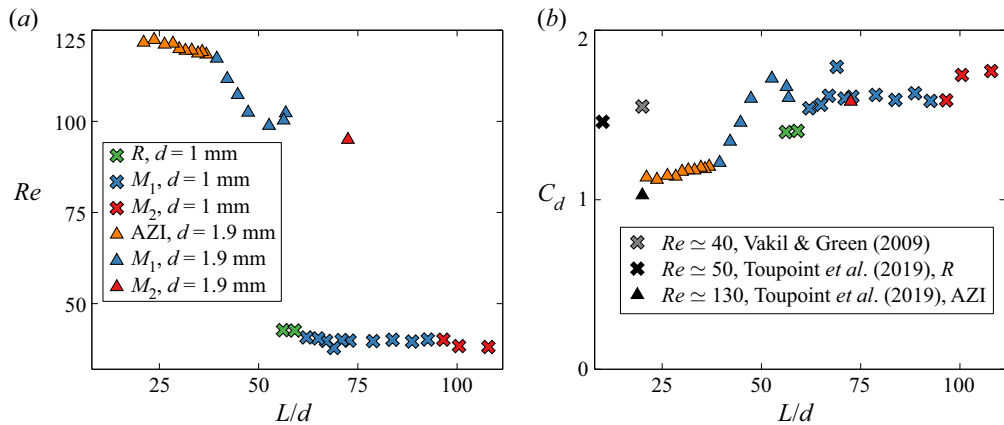
905 R5-5

FIGURE 3. (a) Reynolds number *Re* and (b) drag coefficient C_d as functions of the elongation ratio L/d for $d = 1$ mm (crosses) and $d = 1.9$ mm (triangles): rectilinear motion *R* (green); azimuthal rigid-body oscillatory motion AZI (orange); oscillatory deformations M_1 (blue) and M_2 (red). Values of C_d for freely falling rigid cylinders with $L/d = 10$ and 20, and $m^* \simeq 1.16$ from Toupoint *et al.* (2019) (black symbols) and for a fixed rigid cylinder with $L/d = 20$ from Vakil & Green (2009) (dark grey cross).

amplitude 0.15 *d*). Behaviour M_2 is observed until $L/d \simeq 110$, which is the largest elongation ratio considered for this sequence, featuring a displacement amplitude at the cylinder ends of $0.71d$ and a span-averaged value of $0.32d$.

The bending deformations uncovered here feature several remarkable properties. First, they are restricted in a very distinctive manner to the horizontal plane, that is, perpendicular to the mean fall velocity of the body. Associated vertical displacements are considerably weaker, one or more orders of magnitude lower than those observed in the horizontal plane, and correspond to vertical velocity fluctuations less than 10 % of *U*. Such difference between horizontal and vertical oscillation magnitudes is a typical property of freely moving bodies close to the onset of an oscillatory path (see Ern *et al.* 2012) as well as low-*Re* vortex-induced vibrations observed for rigid (Singh & Mittal 2005) or flexible (Bourguet *et al.* 2011) cylinders.

Second, only a considerably weaker rigid-body oscillatory motion is observed here in the horizontal plane (displacement of the centre of gravity by less than 5 % of *d*, an order of magnitude comparable to that of fluctuations arising from tiny imperfections in the experiment).

The third consideration is that a significant decrease in mean fall velocity occurs when shape oscillations appear. The coloured crosses in figure 3(a) show the evolution of the Reynolds number *Re* as the elongation ratio and the behaviour of the body vary. The periodic deformation of the body results in a loss of mean fall velocity, and therefore *Re*, of approximately 5 %–10 % for M_1. No significant change is then observed for M_2. The strength of the loss is related to the amplitude of deformation experienced by the body, the lower mean fall velocity being obtained for $L/d \simeq 70$, for which the deformation is most marked. The nearby plotted values for $L/d = 72$ and 74 correspond to cases presenting a lateral drift of approximately 7 % and interestingly show higher mean vertical velocities than $L/d = 70$, because of their weaker amplitude of oscillation. The periodic deformation experienced by the cylinder therefore results in additional drag. Drag amplification depends on the amplitude of deformation; a comparable

trend was reported for vortex-induced vibrations of rigid cylinders (see e.g. Khalak & Williamson 1999). This behaviour is illustrated in figure 3(*b*), displaying the drag coefficient associated with the mean vertical velocity of the body, $C_d = (\pi/2)(V_g/U)^2$, obtained by balancing buoyancy and mean drag. Values from Toupoint *et al.* (2019) for freely falling rigid cylinders with $m^* \simeq 1.16$ (black symbols) and from Vakil & Green (2009) for fixed rigid cylinders (dark grey cross) are also displayed, for comparison purpose.

A step forward in the understanding of flexible-body behaviour is achieved from the analysis of the frequencies associated with the periodic deformations. Recordings were carried out on long time series (more than 20 oscillation cycles) and frequencies could thus be determined accurately based on fast Fourier transform. The oscillatory deformations are dominated by a single frequency, except in some transition regions that will be discussed in the following. Furthermore, both cylinder ends are remarkably synchronized, displaying the same frequencies and phase difference over the whole recording.

The deformation frequency f of the freely falling cylinder is plotted as a function of the elongation ratio in figure 4(*a*), for M_1 (blue crosses) and M_2 (red crosses). These frequencies can be compared with the natural frequencies of the bending modes i of an unsupported cylinder with free ends immersed in still fluid. Using a linear Euler–Bernoulli beam model and including added-mass effects (with an added-mass coefficient equal to 1) lead to the bending mode frequencies, $f_i = \alpha_i f_0$, where the constants α_i are related to the roots of the equation $\cosh \beta_i \cos \beta_i - 1 = 0$ by $\alpha_i = \beta_i^2/(8\pi)$, giving $\alpha_1 \simeq 0.890$, $\alpha_2 \simeq 2.454$, $\alpha_3 \simeq 4.811$, $\alpha_4 \simeq 7.952$, ... At a given time t, the corresponding deformed shape of the cylinder for mode i can be expressed in the form $z_c \sin(2\pi f_i t + \phi_i)$, where ϕ_i is a constant phase and the amplitude z_c depends on the longitudinal coordinate x along the cylinder axis as

$$z_c = \cos(\beta_i x/L) + \cosh(\beta_i x/L) + K[\sin(\beta_i x/L) + \sinh(\beta_i x/L)] \qquad (3.1a)$$

$$\text{with} \quad K = [\sin(\beta_i) + \sinh(\beta_i)]/[\cos(\beta_i) - \cosh(\beta_i)]. \qquad (3.1b)$$

Note that for all modes i the integral of z_c between 0 and L is zero, so that the position of the centre of gravity of the cylinder in this model equation does not evolve in time. The frequencies f_i with $i \in \{1, 2\}$ are plotted with thin dashed lines in figure 4(*a*) for mode 1 (blue) and mode 2 (red), showing the correspondence between the succession with L/d of the vibrational modes f_i and the experimental observations. The envelopes of the first two modes provided by (3.1) are also superposed (thick black dashed lines) on the deformed states of the cylinder determined experimentally at different times in figure 2, yielding again good agreement.

Comparing now the deformation frequency f with the inertial time scale associated with the body free fall d/U, which is also the characteristic time scale for vortex shedding about the body, provides values of fd/U varying in the range 0.105–0.140. These values are close to the Strouhal number value, $St_w = 0.105$, associated with subcritical vortex shedding downstream of a long cylinder determined by Buffoni (2003) for $Re = 42$ by slightly vibrating the cylinder to trigger the flow. The wake frequencies $f_w = St_w U/d$ extracted from Buffoni (2003) using the Reynolds numbers corresponding to each L/d in our experiments are drawn with filled circles in figure 4(*a*); these values are close to the measured deformation frequencies. Figure 4(*b*) summarizes the comparison between the frequencies. The data points (blue crosses for M_1 and red ones for M_2) indicate the evolution of the body deformation frequency, f, normalized with the proper bending frequency of the cylinder, f_0, as a function of U^*. The wake frequencies f_w (also normalized
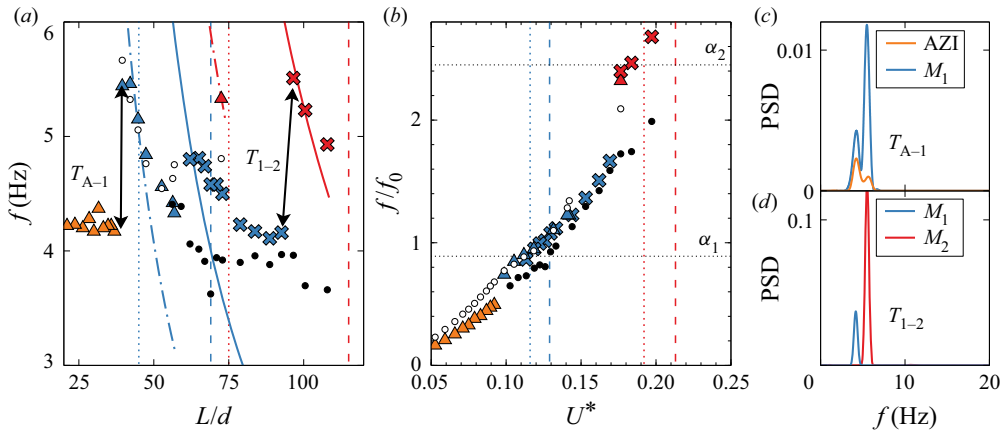
FIGURE 4. (*a*) Deformation frequency f of the freely falling cylinder for M_1 and M_2; natural frequencies f_i (solid lines for $d = 1$ mm, dashed–dotted lines for $d = 1.9$ mm); frequency of AZI for $d = 1.9$ mm. Crosses and triangles: same convention as in figure 3(*a*). Open and filled circles: f_w from Williamson & Brown (1998) and from Buffoni (2003), respectively. Coloured dashed ($d = 1$ mm) and dotted ($d = 1.9$ mm) vertical lines: values of L/d corresponding to $f_i = f_w$ for mode 1 (blue) and mode 2 (red) according to (4.1). (*b*) Frequencies f and f_w normalized with f_0 as functions of the velocity ratio U^*. Horizontal lines: values of α_i. Vertical lines: values of U^* corresponding to those of L/d in (*a*). (*c,d*) Main frequency content: (*c*) near the transition T_{A-1} from AZI to M_1 for $Re \simeq 120$, $L/d \simeq 37$ (orange) and $L/d \simeq 39$ (blue); and (*d*) near the transition T_{1-2} from M_1 to M_2 for $Re \simeq 42$, $L/d \simeq 95$ (blue) and $L/d \simeq 98$ (red).

with f_0) obtained from Buffoni (2003) are drawn with filled circles. We can see that the deformation frequency of the freely moving cylinder is locked to the wake frequency. As L/d varies, the deformation frequency departs from the natural frequencies of the cylinder, indicated by horizontal lines at α_i. At a given stage, however, the next mode of the cylinder is excited and a frequency jump occurs, as can be seen here between M_1 and M_2. For all the L/d investigated, the close agreement of the deformation frequency with the wake frequency suggests that the bending deformations observed are linked to the wake unsteadiness. Furthermore, the results indicate that the cylinder degrees of freedom in deformability allow wake instability to be triggered below the threshold for fixed rigid bodies, as the present Reynolds-number values ($Re \simeq 40$) would be subcritical in the rigid-body case (Inoue & Sakuragi 2008). This point will be discussed further in § 4.

The second situation investigated is that of a freely falling cylinder displaying a periodic motion in association with an unsteady wake. For that purpose, a higher Reynolds number is considered, namely $Re \simeq 120$, obtained for cylinders with $d = 1.9$ mm (figure 3a, triangular data points). At this Re, a rigid-body azimuthal oscillation (termed AZI in the following) of the flexible cylinder is observed from $L/d \simeq 21$ to $L/d \simeq 37$. It corresponds to the azimuthal oscillation reported by Toupoint *et al.* (2019) for rigid cylinders with $L/d = 20$, $m^* \simeq 1.16$, $Re \simeq 130$ and $Re \simeq 220$. In both cases, this rotational oscillatory motion features reproducible low-amplitude (approximately $0.2°$) oscillations of the azimuthal angle of the cylinder, on top of irregular weak displacements comparable to those observed for the rectilinear path at $Re \simeq 42$. As shown in figure 4(*a*) (orange triangles), the AZI oscillation occurs at a frequency of approximately 4.2 Hz. This corresponds to a Strouhal number of 0.13, which is slightly smaller than that of the Bénard–von Kármán instability about a fixed cylinder at this Re, $St_w \simeq 0.17$, obtained from

the relation proposed by Williamson & Brown (1998). Using dye visualization, Toupoint *et al.* (2019) showed that the AZI motion is coupled with an unsteady wake (see their figure 17*c*), similar to those for fixed long cylinders referred to as 'Type II' by Inoue & Sakuragi (2008) and as 'oblique vortex shedding' by Williamson (1989). However, for the freely moving cylinder, a periodic beating of the wake was observed near the body ends, at the oscillation frequency of the azimuthal angle, and in phase opposition between the two ends.

Now, for $L/d \simeq 39$, we observed that mode 1 oscillatory deformations (i.e. M_1) set in. Behaviour M_1 is further observed until $L/d \simeq 57$, the largest elongation ratio that could be investigated for this cylinder. The highest amplitude of deformation is reached for $L/d \simeq 52$, with a displacement of the cylinder ends of $0.8d$ and a span-averaged value of $0.39d$. Note that, in this case also, higher mode responses are expected to exist. Mode 2 deformations were in fact observed for a different cylinder having slightly smaller diameter ($d = 1.8$ mm) and larger length ($L = 131$ mm), i.e. $L/d \simeq 73$. This sequence of deformations shares the properties described in the previous case, in particular the significant velocity decrease and associated drop in *Re* (figure 3*a*, triangular data points). The resulting increase in drag is conspicuous in figure 3(*b*) (triangular data points). For this case also, the proximity between the wake frequency f_w determined from the expression $St_w(Re)$ proposed by Williamson & Brown (1998) (open circles), the cylinder natural frequency f_i (dotted curves) and the observed deformation frequency f (triangular data points) is manifest in figure 4(*a*) and (*b*).

In this second situation, the oscillatory deformations supplant an oscillatory rigid-body motion (i.e. AZI). For sufficiently short flexible cylinders, vortex shedding is coupled with a rigid-body vibration of the cylinder. This corresponds to cylinder ends moving in phase opposition, a property shared with M_2 but conflicting with M_1. Deformation M_1 is nevertheless triggered for a slightly longer cylinder. Closer examination of the main frequency content of the body displacement near the onset of M_1 reveals that the transition features mixed responses: the oscillatory deformation and the rigid-body motion coexist for both $L/d \simeq 37$ and $L/d \simeq 39$, as can be seen in figure 4(*c*). The rigid-body motion predominates in the former case, whereas it is outweighed by the deformations in the latter, and disappears as the elongation ratio is increased further. Note that coexistence of M_1 and M_2 was not detected here in the measurements for $L/d \simeq 95$ and $L/d \simeq 98$ close to the transition T_{1-2} from M_1 to M_2 for $Re \simeq 42$ (figure 4*d*), while superposition of deformation modes is commonly observed for a flexible cylinder held from its ends (Chaplin *et al.* 2005; Huera-Huarte, Bangash & González 2014).

4. Concluding remarks

We investigated experimentally the behaviour of an elongated flexible cylinder settling at moderate Reynolds number under the effect of gravity in a fluid otherwise at rest. For a given cylinder diameter, the experimental approach consisted in gradually decreasing the body length, thereby changing its natural deformation frequency without significantly impacting its mean falling velocity in the absence of deformation. Short enough cylinders behaved like rigid bodies, showing no detectable reconfiguration, and fell with their axis perpendicular to gravity. However, for longer cylinders and therefore higher velocity ratios U^*, the experiments brought to light the springing up of periodic oscillatory deformations of the freely falling flexible cylinders in specific parameter ranges. To the best of our knowledge, the only counterpart of this phenomenon in the literature concerns freely rising bubbles, as discussed in the introduction.

We further showed that the sequence of oscillatory deformations emerging when the cylinder length is increased involve the bending modes of an unsupported beam with free ends, each mode being associated with a natural frequency f_i. Besides, comparison of the deformation frequency with the vortex shedding frequency f_w expected for a non-deformable cylinder at the same Reynolds number indicated that the deformations are coupled with wake unsteadiness. Flow-induced bending deformations involving mode i are expected to occur during free fall when f_i is close to f_w. The simple criterion matching bending mode natural frequency to vortex shedding frequency, $f_i = f_w$, corresponds to

$$L/d = \sqrt{\alpha_i/(USt_w)}(E/(\rho_c + \rho_f))^{1/4}. \tag{4.1}$$

For a cylinder of diameter d, this expression can be used to obtain a prediction of L/d associated with mode i by assuming $U = V_g$ (or $C_d = \pi/2$), which allows one to determine Re and subsequently St_w ($St_w \simeq 0.1$ and 0.17 for $d = 1$ and 1.9 mm, respectively). Corresponding estimations for L/d and U^* are reported in figure 4(*a*) and (*b*) for modes 1 and 2 (vertical blue and red lines) and appear consistent with experimental observations. From (4.1) we can expect the occurrence of higher-order bending modes, for instance in the $d = 1$ mm case for $L/d \approx 162$ (M_3) and $L/d \approx 208$ (M_4).

The experiments also revealed that the oscillatory deformations can develop for distinct flow configurations. Bending oscillations for a freely falling cylinder are here shown to appear for bodies displaying a rectilinear path with a steady wake, and for bodies displaying a rigid-body oscillatory motion coupled with an unsteady wake. In the former case, the close agreement between deformation and wake frequencies suggests that the bending deformations that replace the rectilinear fall are also related to wake unsteadiness, though the Reynolds number would be subcritical in the rigid-body case ($Re \simeq 40$). This indicates that deformability may allow wake instability to be triggered below the threshold corresponding to fixed rigid bodies. The anticipation of wake destabilization due to degrees of freedom of the body has been observed for closely related problems of fluid–body interaction. For instance, Cossu & Morino (2000) and Meliga & Chomaz (2011) investigated the global stability and the nonlinear dynamics close to the threshold of vortex-induced vibrations in the wake of a damped, spring-mounted, circular cylinder. They demonstrated the role of the natural eigenvalue of the cylinder-only system on triggering subcritical vortex shedding at low solid-to-fluid density ratios. In the case of freely moving rigid bodies having different geometries, theoretical and computational studies also revealed that the coupling between the degrees of freedom of the body and the fluid can shift the thresholds and frequencies associated with wake instability about the fixed body or in contrast give rise to different regimes of path instability (Tchoufag, Fabre & Magnaudet 2014; Mathai *et al.* 2017). For instance, in the limit of heavy plates, Assemat, Fabre & Magnaudet (2012) found that the threshold of path instability matches that found for a fixed plate, whereas it decreases when the solid-to-fluid mass ratio decreases, while keeping Strouhal-number values comparable with those of the fixed plate. The present observations provide experimental evidence of the destabilization of a coupled solid–fluid system at a frequency characteristic of vortex shedding, and for Reynolds numbers that are subcritical in the fixed rigid-body case, with the novelty that the degrees of freedom in deformability of the body are involved here. In the second flow configuration, oscillatory bending deformations develop for bodies displaying a periodic motion coupled with an unsteady wake. Except very close to the threshold, the cylinder response to wake forcing becomes essentially a deformation, which takes over the rigid-body displacement of the body. In turn, as the displacements of the cylinder ends shift in this case from
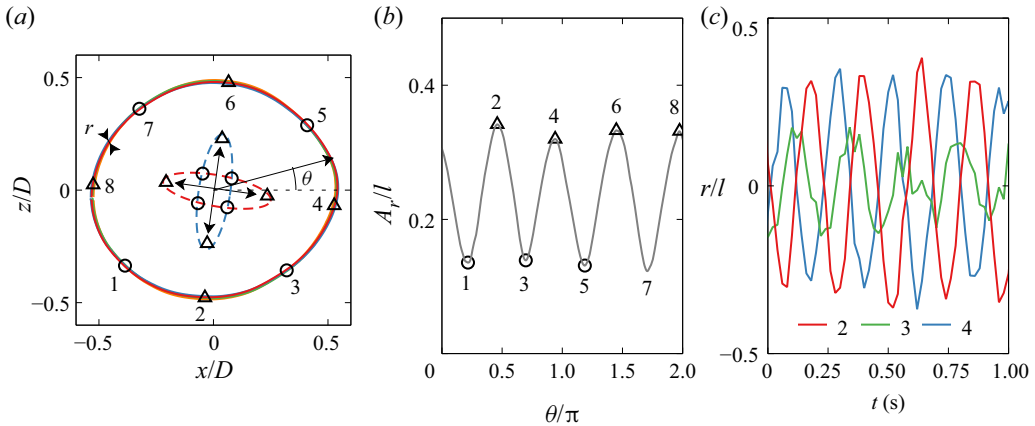
905 R5-10

FIGURE 5. Deformation at a frequency $f \simeq 4.5$ Hz of a thin flexible ring freely falling at approximately 5 cm s^{-1} in water at rest (ring diameter $D \simeq 7$ cm, square-section width $l \simeq 1.5$ mm), corresponding to $Re \simeq 75$ (based on l). (*a*) Ring shape in the horizontal (x, z) plane at several times t. The central inset shows a sketch of the deformation with magnified displacements. The local radial displacement about the time-averaged deformation is denoted r, A_r is the corresponding amplitude and θ is the azimuthal angle. (*b*) Normalized amplitude A_r/l spanned along θ. (*c*) Temporal evolutions of r/l for crest points 2 and 4 and for node point 3.

phase-opposition to in-phase motion, it leads to a change of wake structure, which still needs to be explored.

A major issue now regards the identification and characterization of the wake structures associated with the different deformation modes. The detailed interaction between the flow and the deforming body remains also to be elucidated, in connection with the different amplitudes of deformation that emerge. We are currently heading in that direction, the challenge being to be able to capture both the body and the flow structure over the two orders of magnitude of length scales involved in the problem (spanning from d to L). At issue here is also a better understanding of the role of the cylinder free ends. As observed for freely falling deformable plates by Tam (2015), deformation may concentrate on the body periphery, where the flow field distribution is likely to trigger it. The degrees of freedom in translation and rotation associated with the cylinder free ends may also play a role in deformation phenomena, in the same way they enable the occurrence of oscillatory paths for finite-length rigid cylinders different from those observed for two-dimensional cylinders. As a first step to address this question, we carried out preliminary experiments with flexible rings in a comparable range of parameters. They brought to light oscillatory deformations of the ring at a nearby frequency, illustrated in figure 5; this indicates that also in a closed configuration (i.e. in the absence of end effects), the degrees of freedom in deformability of the body can be excited by the surrounding flow and can couple with it.

Acknowledgements

P. Ern, J. Mougel, S. Cazin, M. Lorite-Díez and R. Bourguet

Declaration of interests

The authors report no conflict of interest.

References

Assemat, P., Fabre, D. & Magnaudet, J. 2012 The onset of unsteadiness of two-dimensional bodies falling or rising freely in a viscous fluid: a linear study. *J. Fluid Mech.* **690**, 173–202.

Bonnefis, P. 2019 Etude des instabilités de sillage, de forme et de trajectoire de bulles par une approche de stabilité linéaire globale. PhD thesis, Université de Toulouse.

Bourguet, R., Karniadakis, G. E. & Triantafyllou, M. S. 2011 Vortex-induced vibrations of a long flexible cylinder in shear flow. *J. Fluid Mech.* **677**, 342–382.

Bourguet, R., Karniadakis, G. E. & Triantafyllou, M. S. 2013 Distributed lock-in drives broadband vortex-induced vibrations of a long flexible cylinder in shear flow. *J. Fluid Mech.* **717**, 361–375.

Buffoni, E. 2003 Vortex shedding in subcritical conditions. *Phys. Fluids* **15**, 814–816.

Cano-Lozano, J. C., Martínez-Bazán, C., Magnaudet, J. & Tchoufag, J. 2016 Paths and wakes of deformable nearly spheroidal rising bubbles close to the transition to path instability. *Phys. Rev. Fluids* **1** (5), 053604.

Chaplin, J. R., Bearman, P. W., Huera-Huarte, F. J & Pattenden, R. J. 2005 Laboratory measurements of vortex-induced vibrations of a vertical tension riser in a stepped current. *J. Fluids Struct.* **21**, 3–24.

Cossu, C. & Morino, L. 2000 On the instability of a spring-mounted circular cylinder in a viscous flow at low Reynolds numbers. *J. Fluids Struct.* **14** (2), 183–196.

Ern, P., Risso, F., Fabre, D. & Magnaudet, J. 2012 Wake-induced oscillatory paths of bodies freely rising or falling in fluids. *Annu. Rev. Fluid Mech.* **44**, 97–121.

Filella, A., Ern, P. & Roig, V. 2015 Oscillatory motion and wake of a bubble rising in a thin-gap cell. *J. Fluid Mech.* **778**, 60–88.

Gedikli, E. D., Chelidze, D. & Dahl, J. M. 2018 Observed mode shape effects on the vortex-induced vibration of bending dominated flexible cylinders simply supported at both ends. *J. Fluids Struct.* **81**, 399–417.

Hua, R.-N., Zhu, L. & Lu, X.-Y. 2014 Dynamics of fluid flow over a circular flexible plate. *J. Fluid Mech.* **759**, 56–72.

Huera-Huarte, F. J., Bangash, Z. A. & González, L. M. 2014 Towing tank experiments on the vortex-induced vibrations of low mass ratio long flexible cylinders. *J. Fluids Struct.* **48**, 81–92.

Inoue, O. & Sakuragi, A. 2008 Vortex shedding from a circular cylinder of finite length at low Reynolds numbers. *Phys. Fluids* **20** (3), 033601.

Khalak, A. & Williamson, C. H. K. 1999 Motions, forces and mode transitions in vortex-induced vibrations at low mass-damping. *J. Fluids Struct.* **13**, 813–851.

Leclercq, T. & de Langre, E. 2018 Vortex-induced vibrations of cylinders bent by the flow. *J. Fluids Struct.* **80**, 77–93.

Mathai, V., Zhu, X., Sun, C. & Lohse, D. 2017 Mass and moment of inertia govern the transition in the dynamics and wakes of freely rising and falling cylinders. *Phys. Rev. Lett.* **119**, 054501.

Meliga, P. & Chomaz, J.-M. 2011 An asymptotic expansion for the vortex-induced vibrations of a circular cylinder. *J. Fluid Mech.* **671**, 137–167.

Mougin, G. & Magnaudet, J. 2002 Path instability of a rising bubble. *Phys. Rev. Lett.* **88**, 014502.

Pfister, J.-L., Marquet, O. & Carini, M. 2019 Linear stability analysis of strongly coupled fluid-structure problems with the Arbitrary-Lagrangian-Eulerian method. *Comput. Meth. Appl. Mech. Engng* **355**, 663–689.

Schouveiler, L. & Eloy, C. 2013 Flow-induced draping. *Phys. Rev. Lett.* **111**, 064301.

Seyed-Aghazadeh, B., Edraki, M. & Modarres-Sadeghi, Y. 2019 Effects of boundary conditions on vortex-induced vibration of a fully submerged flexible cylinder. *Exp. Fluids* **60**, 1–14.

SINGH, S. P. & MITTAL, S. 2005 Vortex-induced oscillations at low Reynolds numbers: hysteresis and vortex-shedding modes. *J. Fluids Struct.* **20**, 1085–1104.

TAM, D. 2015 Flexibility increases lift for passive fluttering wings. *J. Fluid Mech.* **765**, R2.

TAM, D., BUSH, J., ROBITAILLE, M. & KUDROLLI, A. 2010 Tumbling dynamics of passive flexible wings. *Phys. Rev. Lett.* **104**, 184504.

TCHOUFAG, J., FABRE, D. & MAGNAUDET, J. 2014 Global linear stability analysis of the wake and path of buoyancy-driven disks and thin cylinders. *J. Fluid Mech.* **740**, 278–311.

TOUPOINT, C., ERN, P. & ROIG, V. 2019 Kinematics and wake of freely falling cylinders at moderate Reynolds numbers. *J. Fluid Mech.* **866**, 82–111.

VAKIL, A. & GREEN, S. I. 2009 Drag and lift coefficients of inclined finite circular cylinders at moderate Reynolds numbers. *Comput. Fluids* **38**, 1771–1781.

VELDHUIS, C., BIESHEUVEL, A. & VAN WIJNGAARDEN, L. 2008 Shape oscillations on bubbles rising in clean and in tap water. *Phys. Fluids* **20**, 040705.

WILLIAMSON, C. H. K. 1989 Oblique and parallel modes of vortex shedding in the wake of a circular cylinder at low Reynolds numbers. *J. Fluid Mech.* **206**, 579–627.

WILLIAMSON, C. H. K. & BROWN, G. L. 1998 A series in $1/\sqrt{Re}$ to represent the Strouhal–Reynolds number relationship of the cylinder wake. *J. Fluids Struct.* **12** (8), 1073–1085.